Time-resolved studies of electron-hole-droplet transport in Ge

M. A. Tamor, M. Greenstein, and J. P. Wolfe
Physics Department and Materials Research Laboratory,
University of Illinois at Urbana—Champaign, Urbana, Illinois 61801
(Received 7 February 1983)

The interaction of phonons with electron-hole droplets (EHD) in Ge is examined from two points of view: the damping of droplet motion in a force field and the macroscopic droplet motion produced by directed phonon fluxes. The mobility, $\mu=\tau/m$, of the droplets is measured using the strain-gradient method. The magnitude and temperature dependence of the scattering time τ are found to be in agreement with the phonon scattering model of EHD-momentum damping. The phonon-wind force that transports droplets at a velocity V is measurable via the drift relation $F=V/\mu$. The phonon-wind force for a given cw laser excitation is calibrated and compared to that produced by pulsed-laser excitation. In the pulsed case, the wind persists for up to 4 μs after a 100-ns laser pulse, indicating a storage of energy. Time-resolved images reveal a cloud shape very different from the steady-state cloud and show that the phonon storage is localized to within 300 μm of the excitation point. With a simple phonon-wind model, the droplet-velocity data give quantitative information on the energy flux leaving the storage region, and thus the total stored energy. This work demonstrates that electron-hole droplets provide a contactless quantitative probe of nonequilibrium phonon dynamics in Ge at low temperature.

I. INTRODUCTION

The transport properties of electron-hole droplets (EHD) in Ge have been of interest ever since their discovery. The EHD are droplets of a degenerate Fermi liquid of photoexcited electrons and holes that condense at sufficiently low temperature and high excitation levels.[1] In spite of their very large mass, and consequent low diffusivity, EHD travel distances of several millimeters in their 40-μs lifetime. At first it was believed that the drops moved ballistically (coasted) away from their creation point. This interpretation required unphysically long momentum damping times, greater than 10^{-5}s.[2,3] Subsequent theoretical[4-6] and experimental[4,7-9] studies demonstrated that a motive force, produced by nonequilibrium phonon fluxes, was largely responsible for macroscopic droplet motion. The power dependence of the equilibrium size of the droplet cloud was found to be consistent with a model incorporating phonons emitted by hot carrier thermalization near the excitation region.[8,9] Luminescence images showing the EHD cloud shape clearly demonstrated a correlation of cloud features with the phonon focusing patterns in Ge.[9] The sharp cloud features, as well as cloud buildup experiments, showed that the thermalization component of the phonon wind is the dominant motive force for EHD transport in Ge. However, the actual magnitude of this motive force was not quantitatively measured until recently.[10]

The mechanism by which the EHD lose momentum to the crystal is equal in importance to the motive force. It is generally believed that phonon-carrier scattering is the mechanism by which EHD motion is damped. Several techniques have been used to measure the momentum damping time of EHD in Ge although the results differed by over an order of magnitude.[11-13] Ultrasonic measurements[11,12] yielded damping times much smaller than drift measurements.[13] A careful drift experiment which isolated the strain-gradient and phonon-wind forces resolved this disparity.[10] In this paper, we will describe in detail measurements of the phonon-wind force and momentum damping time, τ. We also report a measurement of the temperature dependence of the droplet mobility. This is an important means of identifying the mechanism of momentum damping.

Having characterized the basic transport parameters, τ, and the wind force, we examine the motion of EHD following an intense 100-ns laser pulse. The first time-resolved images of the EHD cloud are presented. These images illustrate the role of anisotropic ballistic phonons in EHD transport, and indicate that the ballistic phonon flux from the localized excitation region persists for several microseconds after the excitation pulse. These results indicate that a portion of the energy deposited by the laser is stored near the excitation point, causing a persistent

phonon emission with a characteristic decay time of about 1 μs. The initial expansion of the electron-hole liquid is observed to be very rapid, suggesting that a single large drop of radius ~ 0.5 mm is formed during and/or immediately after the excitation pulse.

A quantitative understanding of the forces that accelerate and damp droplet motion is of interest by itself. However, for our purposes, knowledge of τ permits the extraction of the net force on each e-h pair in the drop by measuring the drift velocity using the drift relation

$$F = mV_d/\tau \,, \tag{1}$$

where m is the electron-hole pair mass. The phonon-wind strength from various excitation sources can thus be compared by measuring the net forces they produce on electron-hole droplets.

II. EHD MOMENTUM DAMPING

A. Experimental background

The methods previously used to measure τ for EHD in Ge fall into two distinct categories: (1) attenuation of ultrasonic pulses in an EHD cloud[11,12] and (2) time evolution of the EHD recombination luminescence spectrum in a nonuniformly strained sample.[13] The first method extracts τ from the diminution of an ultrasound pulse as it repeatedly passes through the EHD cloud. The principle of the method is quite simple. The sound wave, with wavelength much greater than the drop size, is injected into the sample. Each droplet is accelerated as a whole by the time varying strain field induced by the ultrasonic wave. This motion is damped by carrier interaction with thermal phonons, which carries energy out of the injected wave and converts it to heat. It is the magnitude of this loss rate that is used to determine τ. Early work done by Alekseev *et al.*[11] found a momentum damping time of $\tau = 1.0$ ns at 2.4 K. By a similar method, Hansen[12] found $\tau = 0.8$ ns at $T = 1.8$ K and $\tau = 0.5$ ns at 3.2 K. He extracted τ from the frequency dependence of the ultrasound damping. The results of Hansen are consistent with a T^{-1} temperature dependence in τ, however, the 3.2-K value was not derived from a complete frequency dependence, as was the 1.8-K value.

A strain-gradient method was also employed by Alekseev *et al.*[13] This method took advantage of the band properties of uniaxially strained Ge: A shear strain locally reduces the semiconductor energy gap, thus lowering the e-h pair energy. This effect, upon which our own measurements are based, will be discussed at greater length in Sec. II C. Their experiment was performed on a sample cut into an hourglass shape, square in cross section, and gradually narrowing to a smaller cross section in the middle of the sample. When such a sample was compressed by uniform forces on its flat ends, a shear strain maximum was formed at the narrow "waist" of the sample. EHD created by photoexcitation on an end face moved to the region of lowest e-h pair energy—the strain maximum. Recombination light was collected from throughout the sample. Immediately after an intense 0.1-μs laser pulse, the recombination spectrum was entirely characteristic of EHD near the excitation point (i.e., unshifted). After about 1 μs, however, a second luminescence peak appeared at lower energy, indicating the arrival of EHD at the sample waist (3.5 mm from the excitation point). This velocity, 3.5×10^5 cm/s, combined with an estimate of the energy shift from the sample surface to waist, indicated a momentum damping time of 20 ns at 2.0 K. This value is over an order of magnitude larger than the ultrasound results, raising a serious question whether the two methods were sensitive to the same physical parameter.

B. Theoretical background

The basic method of calculating τ for phonon scattering is now well established. The procedure is analogous to the derivation of the Bloch conductivity result for a simple metal. The electron and hole systems are separate degenerate-Fermi-liquid systems. The motion of a drop is therefore equivalent to the spatial superposition of two currents; the electrons and holes move but no net charge is transported. The carrier-phonon interaction is treated in the deformation potential approximation of Herring and Vogt.[14] The earliest and simplest result for τ in Ge was obtained by Keldysh *et al.*[15]:

$$\frac{1}{\tau} = \frac{2}{3(2\pi)^3}\frac{m_e^2 D_e^2 + m_h^2 D_h^2}{n_0(m_e+m_h)\rho V_s}\left[\frac{k_B T^5}{\hbar V_s}\right] \times \int_0^{\xi_0} \xi^5 \frac{e^\xi}{(e^\xi - 1)^2} d\xi \,, \tag{2}$$

where $\xi_0 = 2\hbar V_s(3\pi^2 n_0)^{1/3}/k_B T$, T is the crystal temperature, ρ is the crystal density, m_e, m_h and D_e, D_h are the mass and deformation potential of the electrons and holes, respectively. The electron-hole–pair density in the EHD is n_0, and V_s is the sound velocity. By setting either the electron or hole mass to zero, the Bloch conductivity result is immediately recovered from Eq. (2). The Keldysh estimate neglected all screening and anisotropy effects, and further required that the carrier drift velocity be

much less than the sound velocity.

It is instructive to compare the Bloch conductivity result for EHD in Ge to that for EHD in Si and also a normal metal, copper. Equation (2) is plotted in Fig. 1, with the temperature scales appropriate to those three systems, using the definition $T_0 = T\xi_0$. We see that, for Ge the damping rate (τ^{-1}) is linear in T above about 1.5 K. For EHD in Si, the $\tau \propto T^5$ regime falls within the ^{4}He cryostat range. Recent experiments by Tamor and Wolfe show this rapid dependence.[16] A simple estimate of the magnitude of the damping time for the EHD in Ge can be gained by treating the electron and hole as a single mass with a single deformation potential. Using $D \simeq 7$ eV,[17,18] and $m = 0.4 \times 10^{-27}$ yields the result

$$\tau = 1.4[T(\mathrm{K})]^{-1} \text{ ns} , \quad (3)$$

for $T \geq 1.5$ K. This estimate is roughly consistent with the calculations of Pan *et al.*[19] and Markiewicz,[20] who calculate $\tau(T)$ for EHD including spatial anisotropies in carrier mass and carrier-phonon coupling. Screening effects were included by different methods in both of these damping estimates, with no more than a twofold decrease in the calculated damping rate. The correction due to screening was comparable to the other errors due to the approximations made in these two calculations. Pan *et al.* estimated $\tau = 1.4\ [T(\mathrm{K})]^{-1}$ ns without screening, and $\tau = 3.0\ [T(\mathrm{K})]^{-1}$ ns when screening is included. Markiewicz concluded $\tau = 1.4\ [T(\mathrm{K})]^{-1}$ ns when screening is included. In both calculations it was assumed that the crystal is unstrained and all the electron energy bands are equally occupied.

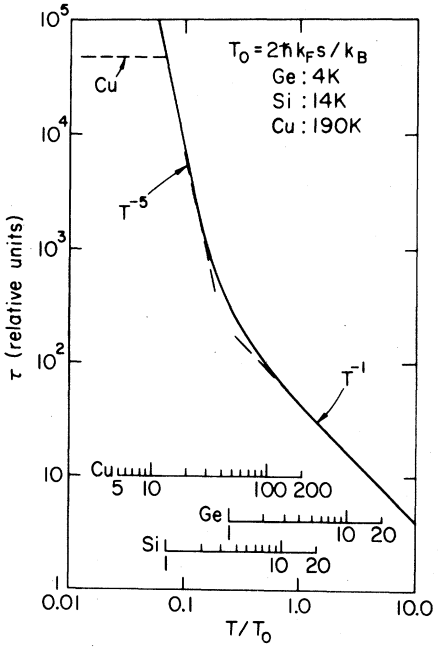

FIG. 1. Temperature dependence of the Bloch conductivity relation [Eq. (2)]. The real temperature is scaled to the reduced temperature, T/T_0, by the Fermi wave vector of the conducting carriers, k_F and the phonon velocity, s. The dashed line indicates mobility saturation in ordinary Cu metal.

Unfortunately, these more elaborate damping calculations have not yet been generally extended to EHD in uniaxially strained Ge, which corresponds to our experimental situations. Markiewicz did evaluate τ for Ge strained along the [111] axis with drop motion along a $\langle 100 \rangle$ axis.[20] The EHD show a twofold decrease in their mobility in this case. Since only one band is occupied the damping becomes anisotropic with respect to the drift direction. The T^{-1} dependence of τ remains unchanged. A determination of $\tau(T)$ in strained Ge will therefore be comparable to the available calculations only in the temperature dependence.

The simplified model, Eq. (2), is extended in Ref. 21 to include the effects of drift at near-sonic velocities. This estimate expresses the force, F, required to maintain a reduced velocity, $\beta \equiv V_d / V_s$, as a function of β and temperature T. At very low temperatures ($\xi_0 \gg 1$) this reproduces the Keldysh result[15] only when $\beta \ll 1$. A rapid increase in damping is predicted as $\beta = 1$ is approached. The lower the temperature, the sharper this onset of large damping becomes. However, at higher temperature ($\xi_0 \leq 6$), as in the case for EHD in Ge above 1.4 K, this increase is very gradual, producing at most a 50% reduction of τ at $\beta = 1$. Thus near-sonic effects are not expected to be strong for $\beta < 1$ in Ge. This is in contrast to the strong nonlinearities observed in Si.[16]

C. Determination of $\tau(T)$

The method for measuring τ that we employ is based on the same principles as the strain-gradient method of Alekseev *et al.*[13] The spatial motion of the EHD is directly observed via their recombination luminescence. By measuring the EHD velocity in a calibrated, variable force field we directly determine the drift mobility. The sample was an ultrapure ($N_A - N_D \lesssim 2 \times 10^{11}$ cm^{-3}) dislocation-free Ge crystal $3.5 \times 3.3 \times 2.7$ mm^3 in size. The 3.5-mm edge was oriented along the [111] axis while the 2.7-mm edge was along the [110] axis. The sample was cooled in a liquid-^{4}He immersion cryostat. The electron-hole liquid (EHL) was generated by a Nd:YAG (YAG denotes yttrium aluminum garnet) ($\lambda = 1.06$ μm) on an etched $(1\bar{1}0)$ face. The EHD recombination luminescence ($\lambda = 1.75$ μm) was detected by cooled Ge photodiode at the exit of a

$\frac{1}{2}$-m, $f/5.6$ spectrometer.

Figure 2 is a schematic of the experimental apparatus. For the purpose of alignment, an infrared image of the sample was made with continuous photoexcitation. The collection lens (85 mm, $f/1.5$) focused a 5×-magnified image of the sample onto the spectrometer entrance plane. Between the lens and the entrance aperture (250×250 μm^2) the image was reflected by two orthogonal mirrors mounted on the shafts of precision galvanometer motors. These motors produced horizontal and vertical displacements of the sample image at the spectrometer entrance.

A cylindrical section of a steel ball bearing ($r=2$ cm) was pressed against the (111) face through a Mylar pad of 200 μm thickness, as shown in Fig. 3(a). The Mylar has the effect of producing more uniform and reproducible strain gradients. The opposite face of the crystal was supported by a polished Cu block. While a minicomputer raster-scanned the image across the entrance aperture, a digitized image of the sample was recorded. Figure 3(b) is such an image of the EHD recombination luminescence, showing the spatial distribution of EHD in the sample. From the excitation point, the EHD stream directly along the $[1\bar{1}0]$ axis for about 1 mm. The larger strain gradients deep in the sample then move the EHD too rapidly to contribute substantial intensity to the EHD "streamer" in the image. The intense luminescence directly under the stress contact (top center of the sample) corresponds to a larger strain-confined electron-hole drop (a γ drop) centered on the shear-stress maximum.[22]

The [111] uniaxial strain reduces the degeneracy of the four $\langle 111 \rangle$ conduction-band valleys in Ge. Three valleys are raised in energy while the [111] valley is lowered. When the energy difference of the strain-split conduction bands exceeds the Fermi energy of the electrons in the lowered bands ($E_F^e \sim 2.5$ meV), the ground state of the liquid corresponds to having all electrons in the lowered valley. In EHD where electrons occupy the lowered bands, the drops move toward regions of maximum shear strain, where the band gap, E_g, and thus the e-h—pair energy, is lowest. Thus a gradient in strain produces a motive force that transports the electron-hole drops. It is this strain-gradient force, F_σ, that is used in lieu of an electric field in these mobility measurements. The calibration of $F_\sigma = -dE_g/dx$ is described in Ref. 10, Figs. 1 and 2.

For the measurement of EHD velocity the laser was switched on and off by an acousto-optic modulator with a 150-ns rise time (10%-90%). The laser was turned on for 10 μs at 2-ms intervals. The peak absorbed laser power was typically between 50 and 150 mW. The low duty cycle prevented sample heating and allowed time for data acquisition and signal averaging. The delay between the laser onset and the onset of the EHD signal was measured as a function of EHD propagation distance into the crystal. This gives the EHD drift velocity; $V_d = \Delta x/\Delta t$. A typical set of onset data is shown in Fig. 4.

By measuring the drift velocity as a function of F_σ at $T=1.4$ K and 2.0 K, a linear drift relation

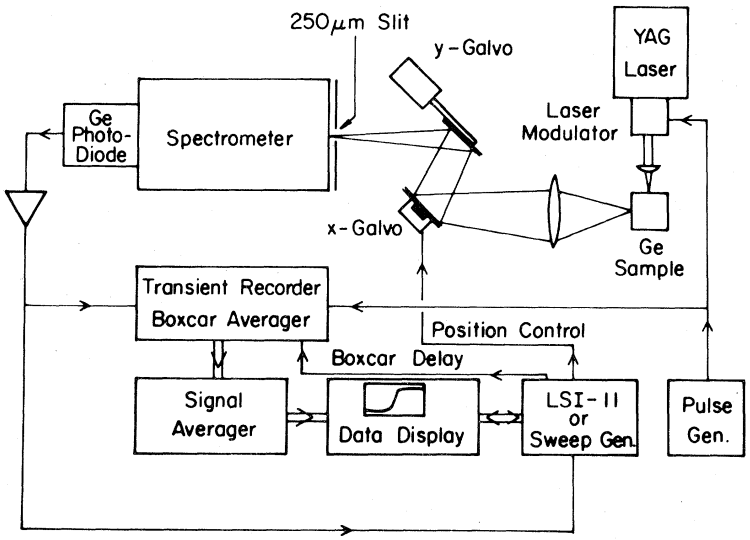

FIG. 2. Schematic for the drift experiment. The exciting laser was switched either by an acousto-optic modulator or an intracavity Q-switch. For imaging, the minicomputer controlled the mirror positions to produce an x-y raster scan, while the boxcar averager selected the desired time interval. For velocimetry the transient recorder was used.

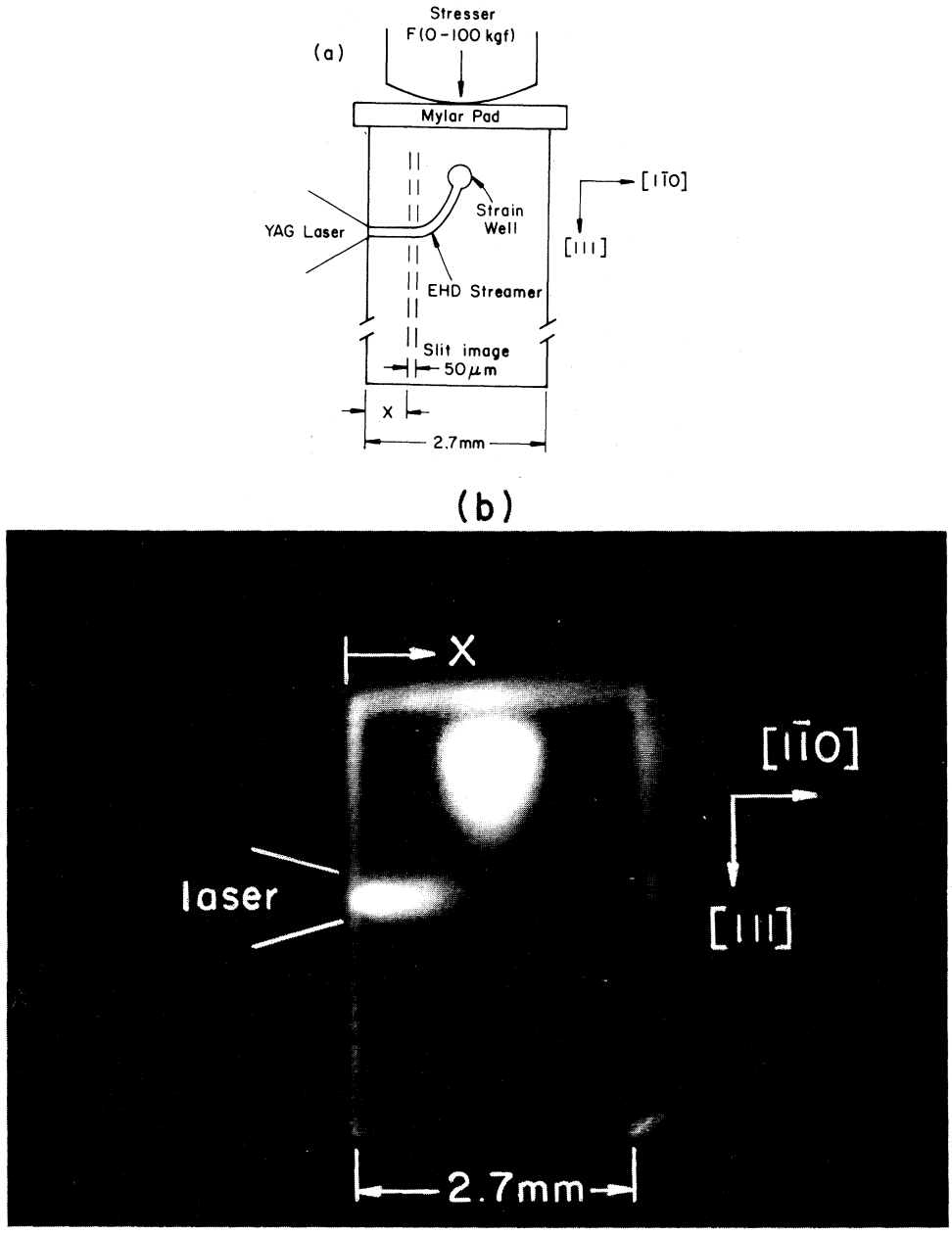

FIG. 3. (a) Schematic of the stress geometry and crystal orientation. (b) Luminescence image of the EHD streamer with low spectral resolution and continuous laser excitation.

was confirmed as shown in Fig. 5. The drift measurements used only the luminescence from positions 300 to 900 μm into the sample. By beginning the velocity determination 300 μm into the sample, near-surface effects due to phonon wind and exciton diffusion were eliminated from these velocity measurements. The droplet velocities were found to be constant over this distance range. The EHD momentum damping time is given by Eq. (1), where m^* is the relevant translational e-h—pair mass: $m^*=m_{et}+m_{hH}=0.43m_0$, where m_0 is the free-electron mass. The correct choice for the hole mass is not immediately clear; uniaxial stress reduces the hole mass. A full calculation of the hole masses in stressed Ge was performed by Kelso.[23] Those results indicate that for $\langle 111 \rangle$ stresses less than 10 kgf/mm^2, a hole near the Fermi surface will have an effective mass of roughly $0.3m_0$ in the $\langle 110 \rangle$ direc-

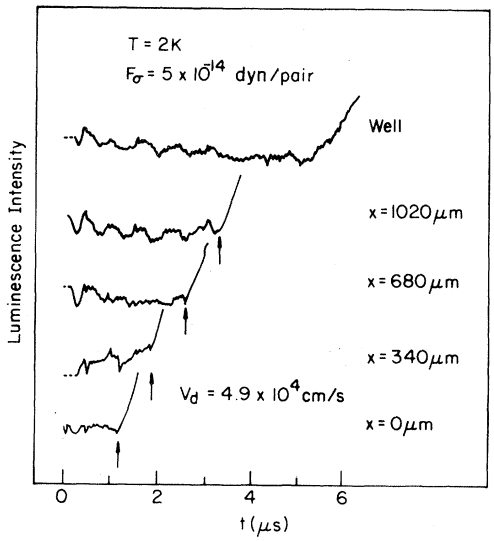

FIG. 4. Set of luminescence transients showing the delay in the appearance of EHD following the laser turn-on. The delay increases as regions deeper in the crystal are sampled. The offset at $x=0$ is produced by delays built into the apparatus.

tion. At larger strains, the hole mass will decrease toward the high-stress limit of $0.14m_0$. For simplicity, we have used the zero-stress hole mass $0.35m_0$ in evaluating τ. The EHD mobility is not sensitive to the choice of hole mass, and is also quoted.

In Fig. 5, the drift velocity extrapolates to $V_d=0$ at $F_\sigma=0$. Therefore, it is not necessary to determine a full V_d vs F_σ dependence for each mobility measurement. Using large strain-gradient forces from 6.0 to 11.0×10^{-14} dyn/pair, the temperature dependence of τ was measured from 1.4 to 2.0 K. Figure 6 shows these results, plotted against inverse

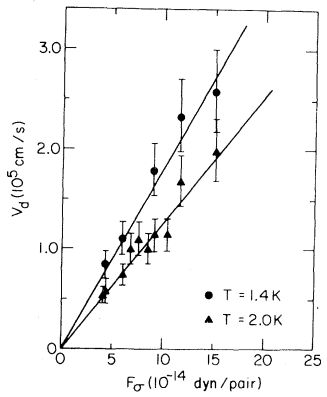

FIG. 5. EHD drift velocity as a function of strain-gradient force, F_σ. The velocity is measured for $300<x<900$ μm. A linear drift relation is observed at both $T=2.0$ and 1.4 K.

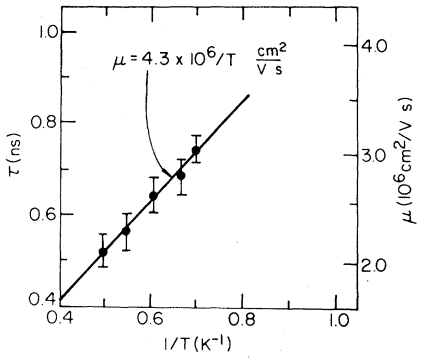

FIG. 6. EHD momentum damping time, τ, and mobility, μ, as a function of inverse temperature in the range 1.4 K $<T<$ 2.0 K.

temperature (T^{-1}). The linearity of this dependence demonstrates that τ obeys a simple T^{-1} law. The fit to the data produced the result (in $cm^2/V\,s$)

$$\mu=v_d/F_\sigma=(4.3\pm0.4)\times10^6[T(\mathrm{K})]^{-1.01\pm0.07}, \tag{4}$$

which gives (in ns)

$$\tau=(1.06\pm0.10)[T(\mathrm{K})]^{-1.01\pm0.07}, \tag{5a}$$

with the translational mass above. If instead, we use the hole mass corresponding to the high-stress limit, we have

$$\tau=(0.54\pm0.05\ \mathrm{ns})[T(\mathrm{K})]^{-1}. \tag{5b}$$

The T^{-1} dependence is exactly as expected from phonon damping of the EHD momentum. Using the measured result, Eq. (4), the magnitude of τ is close to the calculated values and to the earlier ultrasound results.[11,12]

The EHD momentum damping time measured here is about 40 times shorter than that seen by Alekseev *et al.*[13] who also used a strain-gradient method. Those authors observed $V_d\simeq3.5\times10^5$ cm/s for an estimated $F_\sigma\simeq6\times10^{-15}$ dyn/pair, but did not verify the basic drift relation, $V_d\propto F_\sigma$. We suggest that the high drift velocity observed in Ref. 13 is not due to the strain gradient, but rather to a strong phonon wind produced by the intense pulsed excitation used.

III. CALIBRATION OF THE PHONON-WIND FORCE

For unstrained Ge, it has been shown that phonons emanating from the excitation region are largely responsible for the spatial distribution of EHD

within a sample. The force, F_w, actually applied to the drops by this "phonon wind" cannot be directly measured from the droplet distribution. Measurements of drop velocity during cloud growth yield only the product $F_w\tau = m^* V_d$. With the independent determination of τ/m^* from Sec. II C, F_w can be calibrated.

As mentioned earlier, the drift velocities in the strain-gradient experiment were always measured 300 μm or farther from the excitation point. Within this (0—300)-μm region the drop velocity was seen to increase with laser excitation power; the strain-gradient force was augmented by the phonon-wind force. For drop velocities up to $V_d = 2.5\times10^5$ cm/s (i.e., approaching the sound velocity) the drift forces are additive. That is, for an increment in total force δF, the drift velocity will be increased by an amount $\delta V = \delta F \tau/m^*$. This allows the phonon-wind force contribution to the total force on EHD to be measured by direct comparison to the known strain-gradient force. Effectively, we have

$$F_{\rm tot} = F_\sigma + F_w = (V_d + V_w) m^*/\tau \, . \tag{6}$$

The phonon-wind calibration experiment requires only a careful measurement of EHD delay times for positions near the excitation point. With the laser focused to a 100-μm-diam spot, and an absorbed power $P_{\rm abs} = 110$ mW, the EHD onset delay was measured at 90-μm increments in distance, x. Figure 7 shows these results. The droplet velocity is clearly enhanced near $x = 0$, but declines to the constant drift velocity $V_d = 8\times10^4$ cm/s, for the remainder of its flight. A simple geometrical model for $F_w(x)$ is used in fitting the data:

$$F_{\rm tot} = F_\sigma + \Phi P_{\rm abs}/(x^2+\rho^2) \, , \tag{7}$$

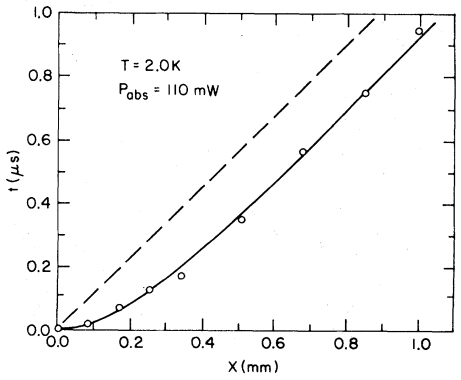

FIG. 7. Arrival time for EHD as a function of position into the sample. The solid line is a fit to Eq. (8). The reduced slope at small x indicates an enhanced droplet velocity near the excitation point. The dashed line represents the delay time expected for zero phonon-wind force.

where Φ is the phonon-wind force strength parameter, and ρ is the laser spot radius. This relation can be inverted analytically and integrated to give the delay time at a given distance:

$$t(x) = \left[x - \frac{\alpha}{(\rho^2+\alpha^2)^{1/2}} \tan^{-1} \frac{x}{(\rho^2+\alpha^2)^{1/2}} \right] \frac{1}{V_d} \, , \tag{8}$$

where $\alpha = \Phi P_{\rm abs}/V_d$. With $\rho = 50$ μm, this relation can be fit directly to the data with only the single adjustable parameter, Φ. The result of the fit is $\Phi = (1.4\pm0.3)\times10^{-16}$ dyn cm^2/pair W, referred to the absorbed Nd:YAG laser power in watts. This measurement was repeated with $P_{\rm abs} = 70$ mW with essentially the same Φ as a result. At 1.4 K, Φ was found to be smaller, such that the product $F_w\tau$ remained constant.

For a point source of phonons the wind force on a drop is, $\Phi P_{\rm abs}/r^2$. For a 40-μs droplet lifetime in unstrained Ge, this predicts a half-intensity cloud radius of $R_c = (0.3\ {\rm cm/W^{1/3}}) P_{\rm abs}^{1/3}$. This is in agreement with the value reported by Greenstein and Wolfe,[9] $R_c = (0.25\ {\rm cm/W^{1/3}}) P_{\rm abs}^{1/3}$. It should be noted that the wind-force calibration does not actually depend on an independent knowledge of τ and m^*. This can be seen by rewriting Eq. (6) as the ratio of forces with and without the wind contribution:

$$\frac{F_\sigma + F_w}{F_\sigma} = \frac{V_d + V_w}{V_d} = \frac{V_{\rm tot}}{V_d} \, . \tag{9}$$

This may be reduced to

$$\frac{F_w}{F_\sigma} = \frac{V_w}{V_d} = \frac{V_{\rm tot} - V_d}{V_d} \, . \tag{10}$$

The ratio τ/m^* appears as the experimentally measured mobility, $\mu = V_d/F_\sigma$, and thus τ alone does not enter into the calibration of F_w. The wind force is actually calibrated here against the spectroscopically measured strain-gradient force.

With the measured value of Φ and μ, it is possible to quantitatively examine other motive forces on the EHD. Through μ, any observed velocity can be directly interpreted in terms of a force, $F = V_d/\mu$. In addition, in the case that this force is due to a nonequilibrium phonon flux, it can be converted to an equivalent continuous-wave (cw) power of absorbed ($\lambda = 1.06$ μm) light. This calibration will be used when we measure the phonon-wind force created by pulsed-laser excitation.

IV. IMAGING OF EHD CLOUD FOLLOWING PULSED-LASER EXCITATION

In examining the transport of electron-hole drops, luminescence images of the drop distribution result-

ing from point excitation have proven to be invaluable. The first images of the steady-state EHD cloud shape in Ge were obtained by Greenstein and Wolfe.[24] These droplet distributions, created by continuous low-power excitation ($P<0.5$ W), showed marked spatial anisotropies correlated with the symmetry axes of the Ge crystal structure and the directions of intense phonon flux.[25] A comparison of the droplet cloud shape and a phonon-propagation pattern revealed the importance of ballistic phonons in establishing the droplet cloud shape. Figure 8(a) is a ballistic phonon image in Ge recorded by Northrop and Wolfe.[25] This image is centered on the ⟨100⟩ crystalline direction and spans 40° left to right in propagation direction. The bright areas correspond to directions of intense phonon flux.

Although isotropically distributed in momentum space ($\vec{k}$ space), thermal phonons from a point source are channeled in real space by the elastic anisotropy of the crystal. The three acoustic modes, slow and fast transverse (STA and FTA) and longitudinal (LA), are each channeled differently. For the transverse modes there exist focusing singularities. These are directions in real space into which a large solid angle in $\vec{k}$ space is directed. These singularities appear as the very bright features in Fig. 8(a). The diagonal $\times$ pattern is due to the FTA phonons, while the wider $+$ shaped feature, with its central "square," is due to STA phonons. The FTA phonons are actually channeled into a narrow ridge 4° wide at [110] centered about the {100} planes. The LA phonons are focused to some extent, but have no singularities and so are not prominent in the phonon image. The focusing of acoustic phonons is discussed at length in Ref. 25.

For comparison, Fig. 8(b) is an infrared image of an EHD cloud excited on a ⟨100⟩ crystal face by 76 mW of continuous-wave laser light. The cloud structure consists of broad "lobes" in a $+$ pattern and sharper "flares" in an $\times$ pattern. These flares are actually due to planes of high droplet concentration seen edge on.[26] It is notable that the directions of high-phonon flux are also directions of greatest spatial extent of the droplet distribution. The sharp features in the steady-state cloud shape [Fig. 8(b)] are due to the corresponding phonon mode in Fig. 8(a). The STA phonons (and the LA phonons) contribute to the vertical and horizontal "lobes" in the cloud shape, while the FTA phonons contribute to the "flares" in an $\times$ pattern.

Our interest in obtaining time-resolved images of the EHD cloud produced by pulsed excitation is motivated in three ways.

First is the general purpose of developing the use of electron-hole drops as a phonon probe. To ac-

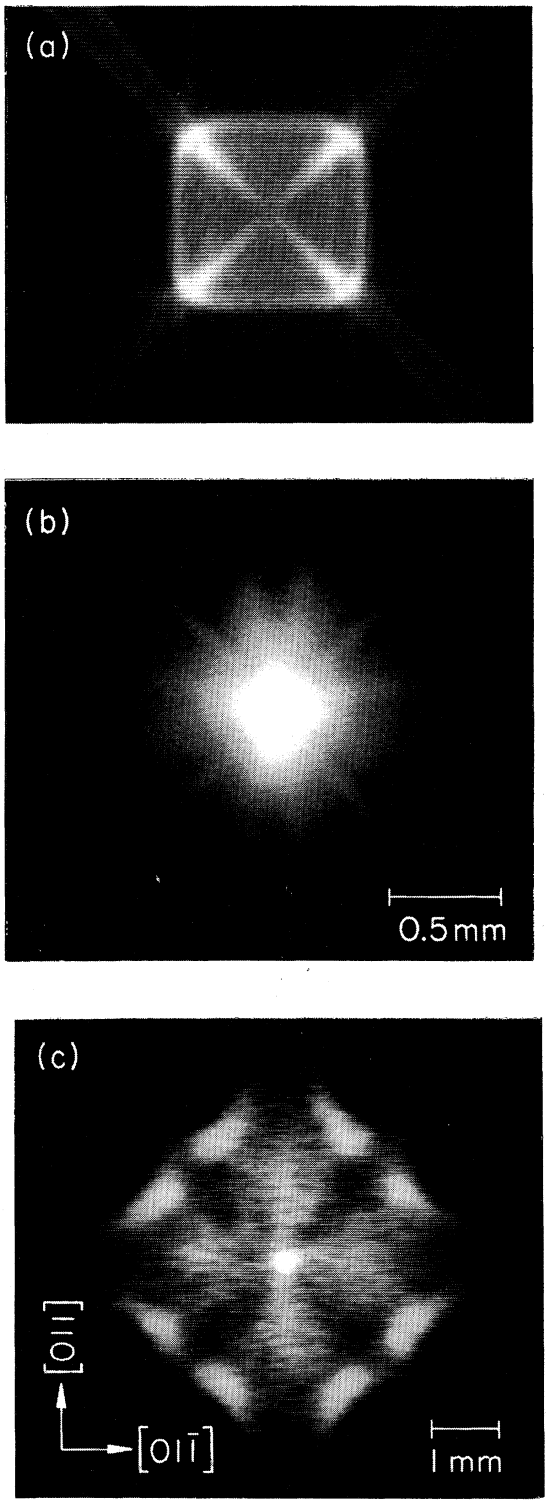

FIG. 8. (a) Ballistic phonon image in the ⟨100⟩ direction from Ref. 25; (b) steady-state ⟨100⟩ cloud image, $P_{inc}=76$ mW; (c) pulsed cloud (300-ns pulse width) taken at 5 μs after the excitation pulse with $E_{inc}=20$ μJ.

complish this aim, droplet velocities must be measured, and these velocities correlated with excitation power.

The second motivation stems from earlier experimental claims indicating that with sufficient photoexcitation intensity drops attain velocities far in excess of the velocity of sound.[3] This would clearly involve forces other than that provided by a phonon wind. In addition, theoretical calculation predicts that a Čerenkov-type emission of phonons, which begins as the sound velocity is reached, will make supersonic motion extremely difficult.[21] We wished to examine EHD motion following intense light pulses in order to characterize the EHD transport processes under such extreme conditions.

The actual details of the cw shape [Fig. 8(b)] provide a third stimulus for this phase of the investigation. The phonon image in Fig. 8(a) indicates the directions of intense phonon flux. Droplets moving in these directions must have velocities greater than those in the low-flux directions. With the assumptions that the initial drop distribution is isotropic and that the same number of drops are moving radially outward in every increment of solid angle about the excitation point, the high-flux directions should correspond to regions of *reduced* luminescence intensity; that is, in the solid angles where drop velocities are higher, the drops will spread over a greater distance in the sample, and the cloud would appear less intense in those directions. This is clearly not the case. Figure 8(b) shows that regions of large-phonon flux are regions of high droplet concentration. This effect requires a "fill-in" process[9] near the excitation point by which the *e-h*—pair distribution remains isotropic in angular direction out to some finite distance from the laser spot. This fill-in effect should not occur for a droplet cloud which was produced by a single intense pulse.

The imaging method is a variant of that described in Sec. II. The sample was a 1-cm cube of ultrapure $N_A \sim 10^{11}$ cm^{-3} dislocation-free Ge. Time resolution is achieved by operating the Nd:YAG laser in a Q-switched mode. This provides (100—300)-ns pulses of up to 100 μJ energy with a 2-kHz repetition rate. A fast current amplifier was placed at the photodiode output. This amplified signal was then fed to a boxcar integrator. The total laser-diode-amplifier system had a 120-ns response time ($1/e$). The luminescence intensity at a selected boxcar gate time was recorded as the sample image was raster scanned across the spectrometer entrance. Approximately 4×10^6 EHD clouds were created to obtain a complete time-resolved image. Figure 8(c) is the EHD cloud shape 5 μs after a 20-μJ laser pulse. The crystal and viewing orientation was the same as in Figs. 7(a) and 7(b). The pulsed EHD cloud has an intricate shell-like structure and shows features that again are correlated with the anisotropic phonon flux. However, in the pulsed case there are dark regions precisely where the bright flares were in the cw cloud.

A complete series of time-resolved images was recorded in the same sample geometry as the images of Fig. 8. Figures 9(a)—9(c) show the EHD distribution at 0.5, 1.0, and 2.0 μs after a 20-μJ, 300-ns focused laser pulse. Figure 8(c) is the 5-μs image from this set. As an aid in interpreting the image data, Fig. 10 presents hidden line drawings of the image intensities at $t=1$, 2, and 5 μs.

In the first image, $t=0.5$ μs, the luminescence is mainly concentrated near the excitation point. However, the EHD distribution already has imbedded in it some anisotropy. At $t=1.0$ μs the prompt-ballistic phonons (those that escape the excitation region immediately upon their generation during the 300-ns pulse) have passed the outward-moving EHD and can no longer participate in droplet transportation. Despite this, the cloud is still rapidly expanding. The $t=1$ μs image shows the developing shell structure. In addition, the anisotropic features are becoming more pronounced.

For the image taken at $t=2.0$ μs, the cloud growth is continuing, but at a slower rate. A shell-like structure which is perforated along directions of high-phonon flux has become apparent by this time. After 5.0 μs [Fig. 8(c)] the expansion of the shell slowed considerably, but the anisotropy features are still prominant. Figure 9(d) is a side view of this cloud at $t=5.0$ μs. The EHD cloud has clearly been driven a considerable distance away from the sample surface.

In order to examine the contribution of different phonon modes to the cloud features, the cloud was excited on a ⟨111⟩ face and imaged along the ⟨111⟩ direction. This time sequence of images recorded at $t=0.25$, 0.5, 1.0, and 3.0 μs with the same laser power as before is shown in Figs. 11(a)—11(d). This sequence again shows the growth of a highly anisotropic structure. The cloud structure in the ⟨111⟩ images of Fig. 10 are dominated by three bright lobes and three darker regions radiating outward.

Recalling the *dark* planar flares in the ⟨100⟩ images of Fig. 9, it is interesting to note that the time-resolved ⟨111⟩ cloud images of Fig. 11 show *bright* axial flares. We believe that this difference is due to the difference in the topology of the two singularity structures. In Fig. 9 the prompt FTA intense phonon flux sweeps out droplets from a very thin planar slice of the cloud structure. This slice is approximately 4° in width. In Fig. 11 the prompt STA intense phonon flux is the same boxlike structure seen in the center of Fig. 8(a), viewed at an angle. The

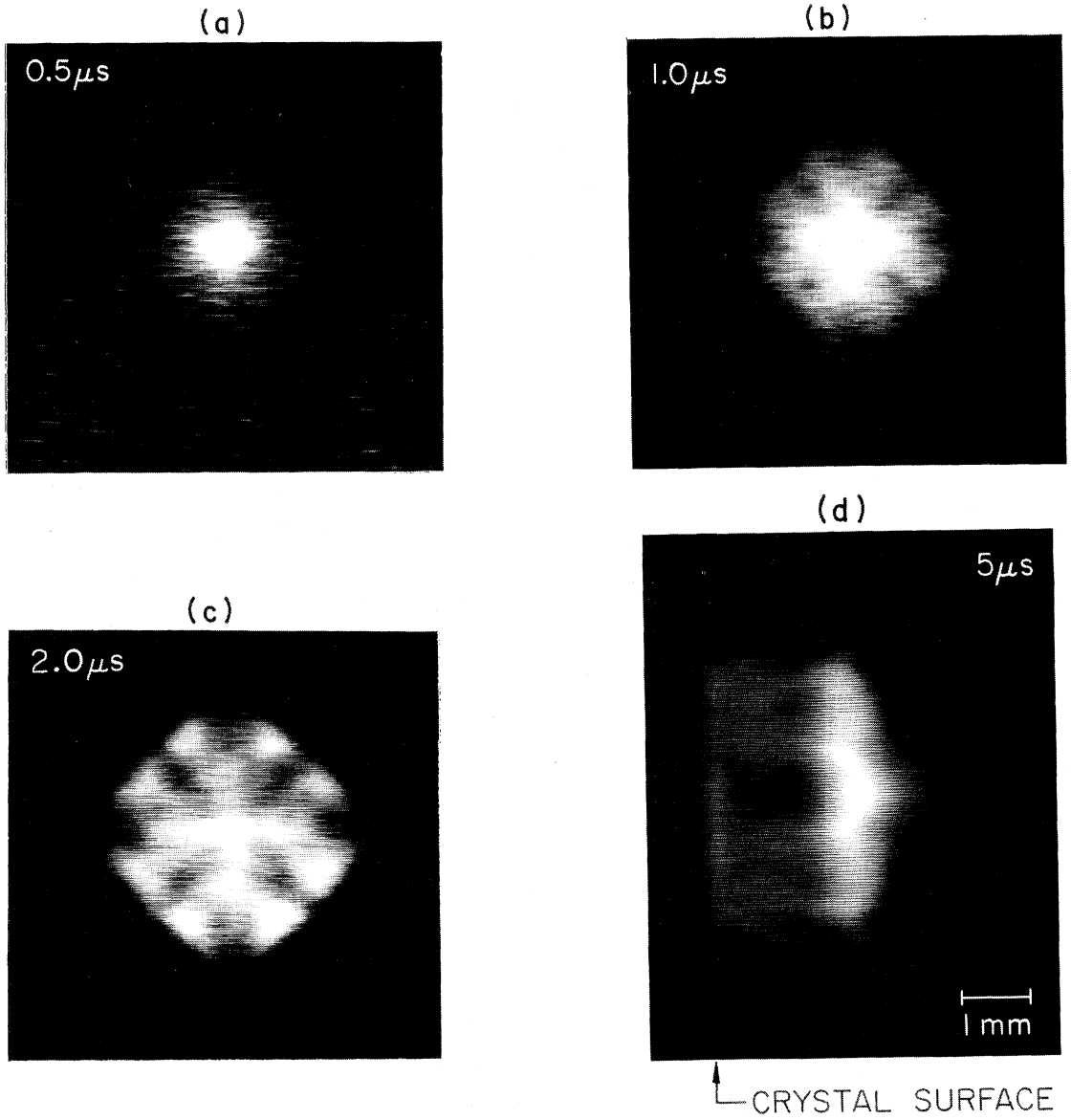

FIG. 9. Time-resolved ⟨100⟩ cloud image for 300-ns excitation. $E_{inc}=20\ \mu J$. (a) $t=0.5\ \mu s$; (b) $t=1\ \mu s$; (c) $t=2\ \mu s$; (d) side view of a time-resolved ⟨100⟩ cloud at $t=5\ \mu s$, $E_{inc}=20\ \mu J$.

most intense phonon flux in Fig. 8(a) is in a square annular region approximately 15° wide which is centered on the ⟨100⟩ axis. This annular flux pattern sweeps out three square annular regions in Fig. 11 and leaves a bright central region along each ⟨100⟩. It is this remaining central structure that is seen as the bright flares in Fig. 11.

In addition to the gross features discussed above, the time-resolved cloud images exhibit intriguing structures for which we have no quantitative description. The droplet intensity is highly dependent on distance and direction from the excitation point. The changes in cloud structure with distance from the center of the images seems even more complex than for the cw images. The cw clouds were remarkably well described by theoretical modeling,[9] and at first thought, the case of a single pulse of droplets expanding into the crystal should present no more difficult a problem. The complexities no doubt arise from the highly nonequilibrium nature of the electronic and thermal energies following an intense laser pulse. Experiments designed to more quantitatively characterize the expansion process are described below. However, a detailed understanding

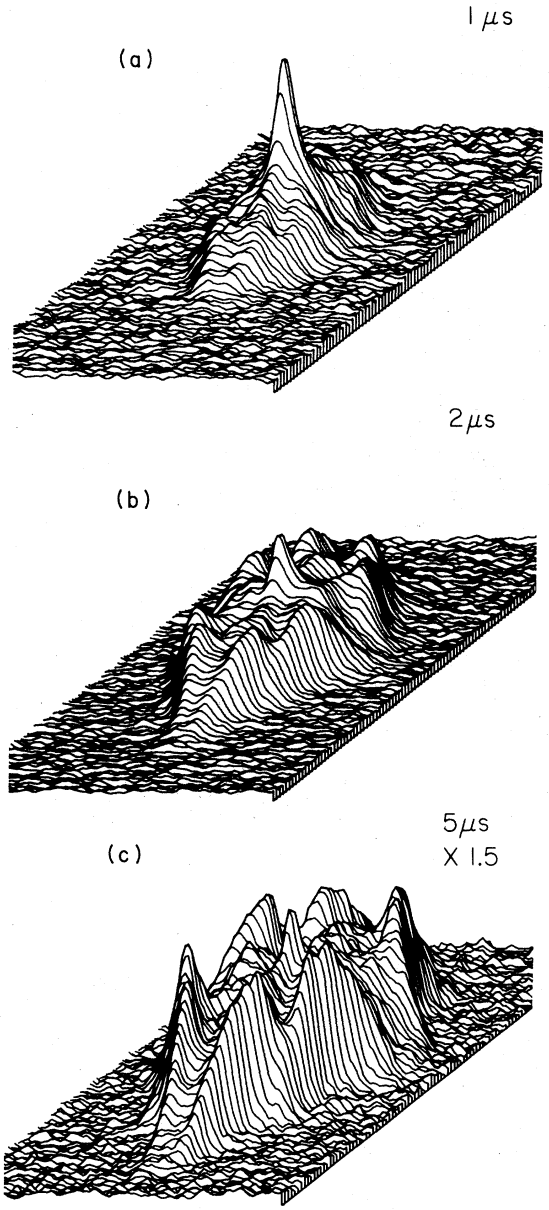

FIG. 10. Hidden line drawings for three of the time-resolved images of Fig. 9. The delay times are given beside each drawing.

of the striking new cloud structures must await future work.

The continued growth of the EHD cloud well after the 300-ns laser pulse is evidence that there is still a localized source of acoustic phonons in the system long after the excitation has ceased. The outward expansion of the EHD cloud indicates that this source of ballistic phonons must lie within the volume defined by the EHD shell. Furthermore, these phonons move the drops in such a way that the cloud anisotropy is enhanced, indicating that the phonon source is quite localized.

The most obvious persistent phonon source is due to the Auger recombination of electron-hole pairs within the drops. This flux of recombination phonons (R wind) produces a force of mutual repulsion between all drops that will persist throughout their 40-μs lifetime. This R wind can be eliminated as the primary phonon source for three reasons. First, it is a diffuse phonon source which would tend to wash out the anisotropic cloud features rather than maintain them. Second, the net outward force on the drops at the inside edge of the shell would be far less (ideally zero) than the force on those on the outside. This effect would tend to spread the cloud shell thickness radially, probably more than observed. Third, an R-wind–driven expansion should continue for the lifetime of the drops. Images recorded for delay times much greater than 5 μs (up to 20 μs) do not show a persistent high-velocity expansion.

We can conclude that the observed cloud growth is somehow related to the thermalization phonons generated at the excitation point. Phonons emerging from the excited region would have the effect of radially expanding the droplet shell without spreading it. As was pointed out earlier, the ballistic phonons generated during the laser pulse will certainly outrun the drops in about 0.5 μs. This indicates that energy has been stored at or near the excitation region. The continued cloud expansion implies that some of this energy is released in the form of acoustic phonons during a total time of about 4 μs. Any substantial spatial broadening of the source of these late phonons would widen the angular width of the phonon singularity features. The rather sharp structures in the final cloud indicate that this persistent phonon source is confined to a region no larger than ~ 300 μm in diameter. This estimate was obtained by comparing the opening angles of the singularity features in the pulsed cloud image to the corresponding angles in the phonon image [8(a)]. The nature of this energy storage will be examined in the next sections.

The question of supersonic motion is not directly addressed by these images. However, it is simple to estimate the initial drop velocity from the cloud extent in the earliest image of each series. In the $\langle 100 \rangle$ view, Fig. 9 shows a cloud ~ 0.6 mm in diameter at $t = 0.5$ μs. This corresponds to a velocity of 6×10^4 cm/s, well under the speed of sound, $V_s \sim 5 \times 10^5$ cm/s. In the $\langle 111 \rangle$ view of Fig. 11(a), at $t = 0.25$ μs, the cloud is larger; ~ 0.8 mm in diameter. This estimates a drop velocity of 1.6×10^5 cm/s, still subsonic.

The questions concerning the cloud "fill-in" effect

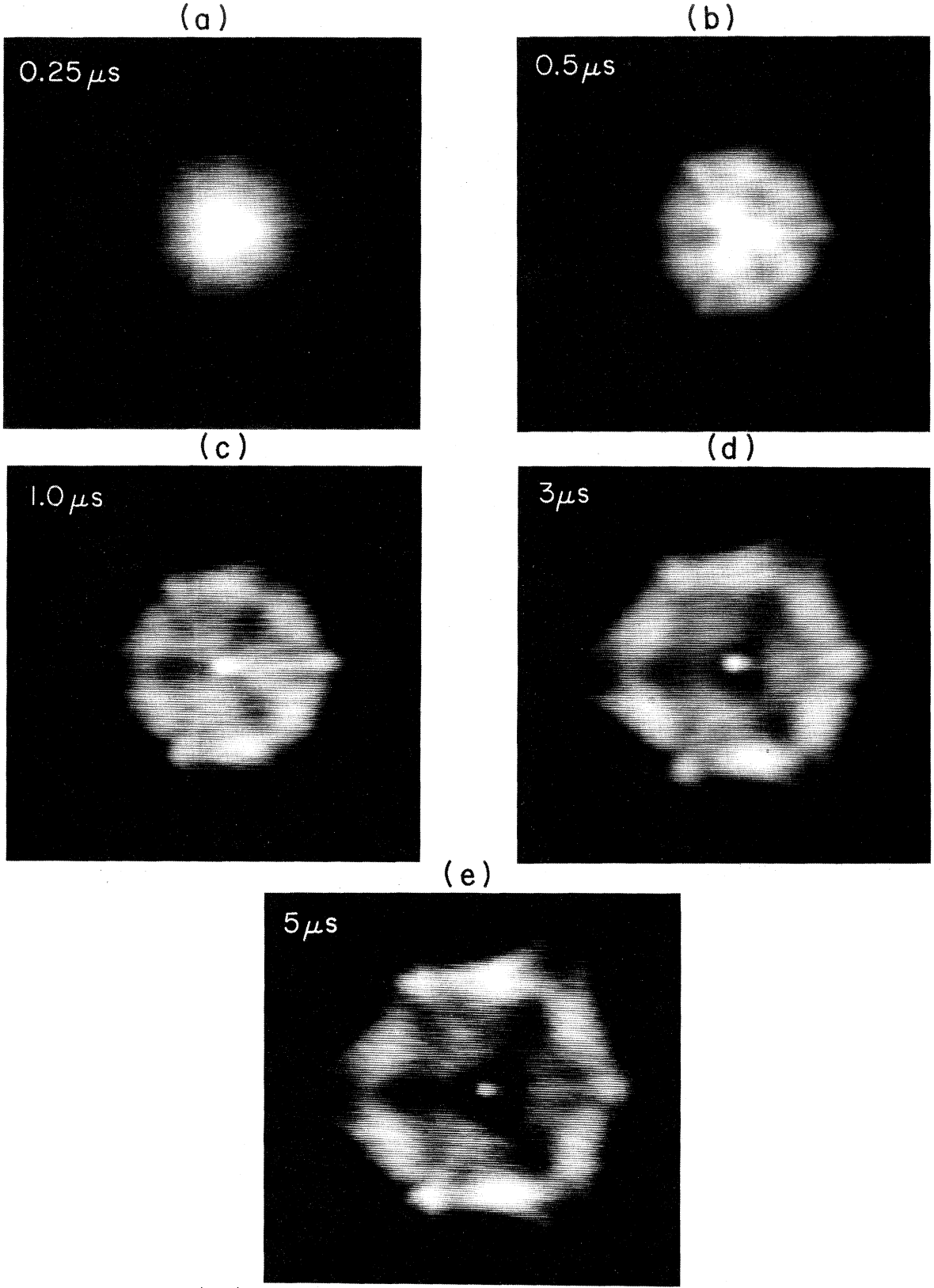

FIG. 11. Time-resolved ⟨100⟩ cloud images for $E_{inc}=20$ μJ. (a) $t=0.25$ μs; (b) $t=0.5$ μs; (c) $t=1$ μs; (d) $t=3$ μs; (e) $t=5$ μs.

are addressed directly by the pulsed data. It has been established that there is a local source of acoustic phonons after the laser pulse. However, without further optical excitation, there can be no further production of electron-hole pairs from which droplets may condense. The time-resolved images show that the directions of high-phonon flux are swept partially clear of droplets which are not subsequently replaced. We conclude that for continuous excitation, in which the directions of high flux are coincident with high-luminescence intensity, these directions are continuously replenished with EHD at the excitation region. This is the postulated fill-in process, present only for cw excitation.

Another possible factor in determining the cloud distribution after intense excitation in evaporation of EHD due to heating. Those droplets initially along high-flux directions absorb more phonons and are more likely to heat up and evaporate. On the other hand, droplets traveling near the sound velocity are postulated to cool themselved efficiently by phonon emission.[21,16] The strain-gradient experiments described previously in this paper showed no evidence of droplet heating or cooling for drift velocities up to $0.5V_s$. Also, experiments described below show no significant loss of luminescence intensity as the average droplet velocities are increased by increasing excitation level. Still, evaporation of EHD due to internal heating should not be completely ignored in this highly nonequilibrium situation.

V. EHD TRANSPORT WITH PULSED EXCITATION

In this section we present more quantitative data on the evolution of the pulse-excited EHD cloud. To obtain these data, and ease their interpretation, a simpler one-dimensional geometry was employed. To produce this geometry, the laser was left unfocused, creating an excitation region 1.8 mm in diameter. A polished (100) surface was excited, while the EHD luminescence light was collected from a perpendicular (110) face (i.e., a "side view"). To maximize light collection in the spectrometer, a vertical entrance slit was used. The image of the sample was then displaced horizontally by a galvo-driven mirror. In conjunction with the boxcar integrator, time-resolved spatial profiles of the luminescence along the $\langle 100 \rangle$ direction of drop motion were obtained. The laser produced at most about 100 μJ in a single pulse, equivalent to 25 mJ/cm^2, well below the threshold for surface melting (~ 1 J/cm^2). The excitation and detection geometry used here is similar to those used in Refs. 3 and 27. However, the time and spatial resolutions of this experiment are superior to those used in the earlier work.

Figure 12 is a series of time-resolved spatial scans taken with 300-ns boxcar gates, and a pulse energy of 15 μJ and width 300 ns. This time resolution is similar to that used in Ref. 3. The sharp peak at each end of the profile is luminescence from throughout the sample which is scattered by imperfections along the crystal edges. The EHD distribution penetrates well into the sample (~ 0.6 mm) even as the laser is still on. This initial distribution grows in intensity and the maximum intensity breaks away from the surface. To interpret these spatial profiles, the positions of the peak, half-maximum, and edge of the EHD distribution [defined in Fig. 12(a)] are plotted as a function of time in Fig. 12(b). As was hoped, these data at reduced time resolution nearly duplicate the results of the previous work.[3,27] In the rest of this section we focus our attention on the half-maximum data.

A large spatial extent of the EHD distribution at early times was previously interpreted as a supersonic motion of EHD from the crystal surface.[3,27] For our data, a crude analysis also implies a drop velocity well in excess of 5×10^5 cm/s. However, there are no data points in Fig. 12, or in Refs. 3 and 27 that show the cloud actually expanding to this size within the system time resolution. It is the extrapolation from the initial distribution back to the sample surface that produces the estimates of very large velocities. The validity of the extrapolation is also questioned in the theoretical work of Pan *et al.*[19] and the experimental work of Zamkovets.[27] By repeating this type of measurement with 100-ns resolution we wished to determine whether the EHD move supersonically from the surface, or actually form deep inside the sample.

For the 100-ns resolution data we present only the half-maximum position as a function of time. Figure 13 shows the cloud size, defined in this way, as a function of times for 100-ns excitation pulses and four values of incident laser energy (8, 20, 37, and 59 μJ), At the three highest powers EHD luminescence appears immediately at 0.4 mm or more into the sample. This corresponds to an initial velocity greater than 6×10^5 cm/s. The subsequent instantaneous velocities are all less than 2×10^5 cm/s and decrease smoothly as the cloud grows. At the low power (8 μJ), the cloud appears to penetrate from the sample surface with a velocity of $\sim 2\times 10^5$ cm/s. For all of the 100-ns resolution data in Fig. 12, any velocity measured between two actual data points after $t=0$ is always well below the slowest speed of sound, $V_{\rm STA}=3.6\times 10^5$ cm/s.

It appears from Fig. 13 that the EHD motion breaks into three regimes: (1) an initial "jump-out" of up to ~ 1 mm; (2) a continued fast expansion at

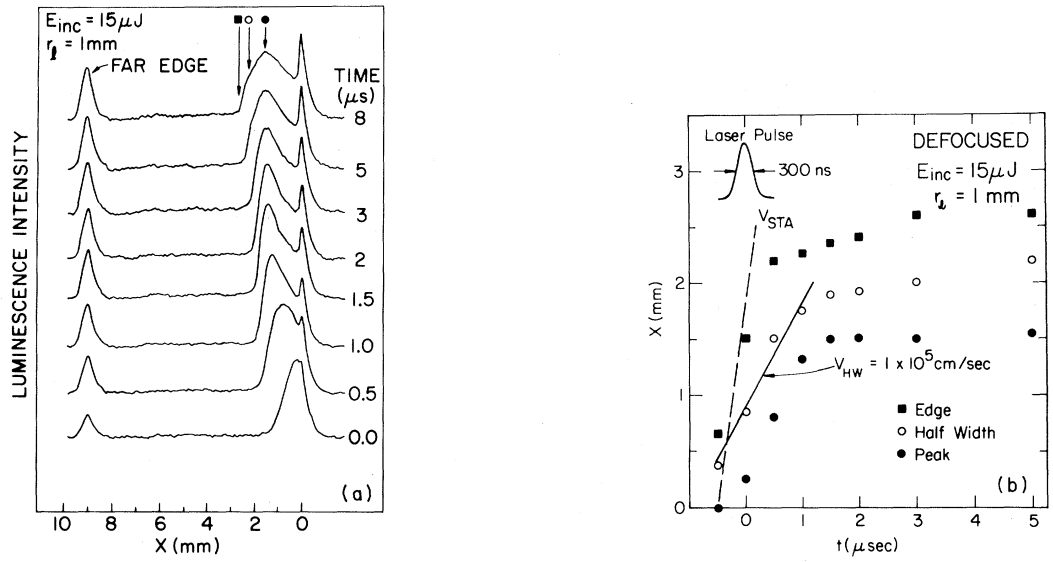

FIG. 12. (a) Time-resolved slit scans for 300-ns defocused excitation on a polished (100) surface at $T=1.8$ K. The intense peaks at $x=9$ mm and $x=0$ mm are from light scattered off of the edges of the sample. (b) Plot of the peak, half-maximum, and edge positions [defined in (a)] as a function of time. In these figures, $t=0$ corresponds approximately to the peak of the laser pulse.

velocities up to $\sim 2\times 10^5$ cm/s, persisting for ~ 1–2 μs; and (3) a much slower expansion with velocities $< 10^4$ cm/s that persists for more than 10 μs.

The very slow expansion of the EHD cloud appears to persist long as drops are present in the sample. At such long delay times after the laser pulse one obvious remaining phonon source is the recombination of the electron-hole pairs. The continued expansion of the clouds imaged in Sec. IV may also be due to this gentle, but persistent phonon flux. Keldysh[5] has estimated the drop velocity produced by this phonon flux and found it to be of order 10^3 cm/s. This is consistent with the observed cloud growth rates well after the excitation pulse. We believe, therefore, that the final slow expansion of the cloud is due to a recombination-phonon wind.

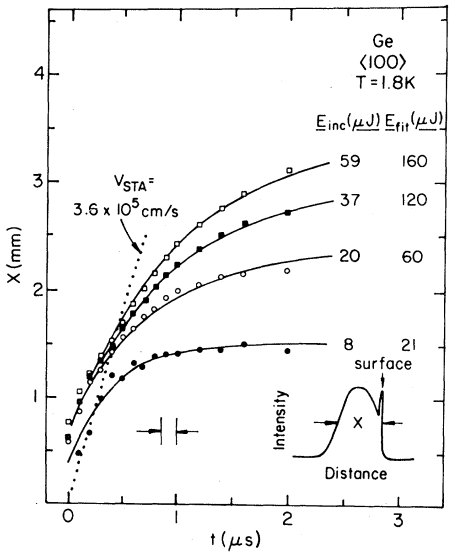

FIG. 13. Time evolution of the spatial profile full-widths for 100-ns defocused excitation on a polished (100) surface. Data points are plotted for four excitation levels, $E_{\rm inc}$. The solid lines are a fit from Eq. (21) with $E_{\rm fit}$ and τ_s as adjustable parameters.

We believe that the initial jump-out can be explained in terms of the formation of a single large drop of electron-hole liquid near the surface. The jump-out is observed at laser energies above about 10 μJ. When the Ge crystal is excited by the defocused 10-μJ Nd:YAG laser pulse, approximately 10^{16} e-h pairs/cm^2 are generated near the sample surface. If the e-h—pair density is higher than the equilibrium density for EHD, the initial carrier distribution will expand to lower its average density. This expansion will be driven both by the outward diffusion of the newly generated carriers, and by the reduction in total energy that is associated with the reduction in pair density. Assuming that the initial distribution rapidly expands until the carrier density drops to $n_0=2.3\times 10^{17}$ cm^{-3}, we estimate the final layer thickness, x_0, as a function of excitation density as

$$x_0 = \frac{E}{\pi \rho_0^2 h\nu} \frac{1}{n_0} , \tag{11}$$

where E is the total energy absorbed on a disk with radius ρ_0 (=0.9 mm) and $h\nu$ is the photon energy. This yields the result (in cm)

$$x_0 = 6 \times 10^2 E_{\text{inc}} , \tag{12}$$

for $E = 0.6\ E_{\text{inc}}$, assuming an absorption factor of 60%, and E_{inc} in joules. For our experimental geometry, and an incident pulse energy of 60 μJ this predicts $x_0 = 0.4$ mm. Figure 14 shows the initial cloud halfwidth, x_0, as a function of incident pulse energy. The figure includes data from both the 300-ns and 100-ns resolution systems. The experimental results are quite consistent with the postulated linear relation between pulse energy and initial drop size. The measured half-width is within a factor of 2–3 of that predicted above, indicating that the initial density is indeed close to that of a single drop.

In their light scattering work, Zamkovets *et al.*[27] observed that EHD first appeared at the edge of the initial carrier distribution. They could not explain this result, and lacked the time resolution to further explore the effect. Combescot[28] has theoretically considered the initial behavior of a pulse-excited *e-h* plasma. She suggests that a very rapid plasma expansion takes place. Rapid growth will continue until the plasma has entirely condensed into an electron-hole liquid. The details of this expansion are strongly dependent on the initial plasma density and temperature.

It is not clear from our data whether a plasma of density greater than the EHL is formed initially. A simple argument may be used to show how such a plasma would affect our results. For EHD in Ge

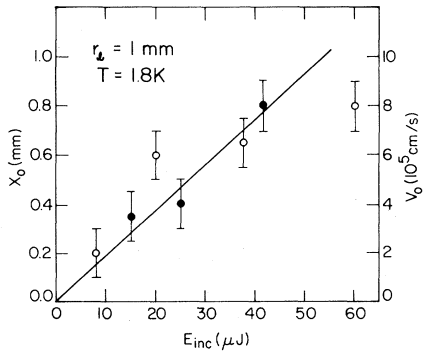

FIG. 14. Plot of the "jump-out" distance, x_0, and computed "jump-out" velocity, V_0, as a function of excitation level. Note that $V_0 = x_0/100$ ns. The slope of the solid line is 2×10^3 cm/J.

Auger recombination is the dominant mechanism in determining the droplet lifetime. Thus, the carrier lifetime will begin to decrease as n^{-2} at higher densities. For sufficiently high *e-h*—pair density, $n \gtrsim 10^{19}$ cm^{-3}, the recombination time will become shorter than the laser pulse duration. In this case, an equilibrium carrier density is achieved during the pulse. It is easy to show that under these conditions the total number of carriers present after the laser pulse increase only as $(E_{\text{abs}})^{1/3}$. Thus the generation of a high-density *e-h* plasma would be evidenced by a sublinear increase in the total volume of EHL generated as the pulse energy is increased. With the possible exception of the point for $E_{\text{inc}} = 60$ μJ, Fig. 14 does not indicate this effect. In addition, we observe no nonlinearity in the total EHD luminescence intensity. It appears that 100-ns pulse excitation simply creates a growing "giant drop" of EHL. This pancake-shaped volume is completely filled by electron-hole liquid, and later breaks into individual electron-hole drops. In this case, the first appearance of small droplets would be deep in the sample, while optical absorption would be observed throughout the EHL volume, as in Ref. 27. In either case, observation of the formation of EHD following a shorter (less than 100 ns) excitation pulse with the same total energy might reveal the nonlinearities associated with a high-density electron-hole plasma. Spectroscopic evidence for supersonic plasma expansion in Si with shorter pulses (15 ns) has recently been reported.[29]

We now turn our attention to the intermediate, rapid-cloud-expansion regime. For the same reasons given in the imaging section, we can conclude that the rapid expansion is due to a flux of acoustic phonons emitted from the excitation region *after* the laser pulse. This phonon storage process has also been observed directly by bolometer detection methods and discussed in detail in Ref. 30. The observed storage times are similar to those found here. In order to quantitatively model the motion of EHD in an intense phonon wind we must confirm that the drop velocity is proportional to the phonon energy flux. To confirm this, the initial droplet velocity after the "jump-out" was measured as a function of incident pulse energy, E_{inc}. These results are shown in Fig. 15(a) for defocused ($r_l = 0.9$ mm) and in Fig. 15(b) for focused ($r_l = 100$ μm) laser excitation. In both cases an initial linear relation is observed; the drop velocity is proportional to the laser power.

Both excitation geometries show a saturation in velocity at high-pulse energy. The initial slopes in Figs. 15(a) and 15(b) are similar in magnitude. However, in the focused case the velocity is seen to saturate at much lower pulse energy. We attribute the velocity saturation in the focused case to the

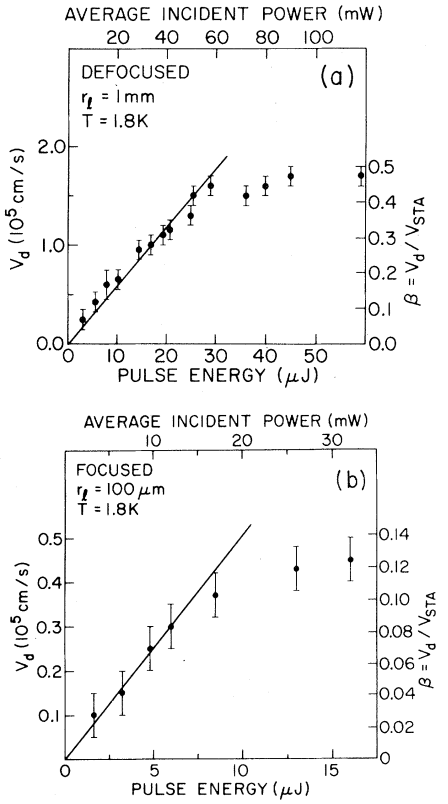

FIG. 15. Power dependence of the maximum EHD velocity illustrating the linear drift relation and velocity saturation effects. (a) defocused ($r_l = 1$ mm) geometry; (b) focused ($r_l = 100\ \mu$m) geometry.

high excitation density involved. The highest value of $E_{\rm inc}$ in Fig. 15(b) is only a factor of 2 below the threshold for visible damage, which requires local melting at temperatures near 1200 K. It seems likely that the phonon wind itself saturates as melting is reached. On the other hand, the energy density for defocused excitation [Fig. 15(a)] is far below the melting threshold. We believe that the velocity saturation in Fig. 15(a) may be due to the reduced efficiency of acoustic phonons in pushing EHD as the drift velocity approaches the speed of sound. This near-sonic force correction will be included in the phonon-wind model in the next section.

VI. PHONON-WIND MODELING

In this section we describe a simple model for the phonon-wind force on an electron-hole drop. This model includes the excitation geometry, the decay of the phonon flux in time, and the effects of near-sonic droplet velocities. The model will be used to generate curves of the cloud size as a function of time after an excitation pulse. These curves are then fit to the experimental results using the phonon-storage time, τ_s, and the incident pulse energy, $E_{\rm inc}$, as fit parameters. It is this procedure that makes the EHD motion study a quantitative probe of the phonon dynamics.

The construction of the cloud growth model begins with the phonon-wind strength parameter, Φ, measured in Sec. III. This parameter calibrated the phonon-wind force for point excitation as

$$F_w(r) = \Phi P_{\rm abs}/r^2 , \tag{13}$$

where $P_{\rm abs}$ is the absorbed cw Nd:YAG laser power, r is the distance from the excitation point, and $\Phi = 1.4\times 10^{16}$ dyn cm^2/pair W. This relation is used as a source function for an arbitrary spatial distribution of laser excitation. For a cylindrically symmetric phonon-source function, which does not vary in time, the net force, $F(x)$, on a drop is given by

$$F(x) = \Phi \int_0^{2\pi}\int_0^{\rho_0} \frac{x}{(x^2+\rho^2)^{3/2}}\sigma(\rho)\,d\rho\,d\theta , \tag{14}$$

where the drop in question lies on the axis of symmetry, a distance x from the phonon source. The power density on the surface is $\sigma(\rho)$, where ρ is the coordinate in the plane of the phonon source.

The time dependence of the phonon source can also be included in Eq. (14), with a correction for the phonon time of flight:

$$F(x,t) = \Phi \int_0^{2\pi}\int_0^{\rho_0} \frac{x}{(x^2+\rho^2)^{3/2}} \times \sigma(\rho)T(x,t)\rho\,d\rho\,d\theta . \tag{15}$$

Here, $T(x,t)$ is the time-dependent form of the phonon source. Based on the observed exponential decay of the phonon flux in bolometer experiments,[28] we will assume that

$$T(x,t) = \exp\{-[t-(x^2+\rho^2)^{1/2}/V_s]/\tau_s\} . \tag{16}$$

The total energy in the phonon system is then

$$E = \int_0^{2\pi}\int_0^{\rho_0} \sigma(\rho)\tau_s\rho\,d\rho\,d\theta . \tag{17}$$

At this point we make two simplifying assumptions: (1) the phonon-source density $\sigma(\rho)$, is uniform on a thin disk of radius ρ_0 and (2) the phonon velocity is large enough that the radial part of the time delay correction may be omitted. The second assumption is justified as the maximum difference in phonon arrival time at the droplet is seen when the droplet is at $x=0$. At $x=0$ the delay between phonons from $\rho=0$ and those from ρ_0 is $\rho_0/V_s = 0.2$ μs where V_s is the phonon velocity. This time is

quite short compared to the storage time of order 1 μs. In addition, the delay effect is reduced as x increases. The force function of Eq. (14) becomes

$$F(x,t)=\Phi\sigma 2\pi\int_0^{\rho_0}\frac{x\rho}{(x^2+\rho^2)^{3/2}}e^{-(t-x/V_s)/\tau_s}\,. \tag{18}$$

This may be integrated to the form

$$F(x,t)=2\pi\Phi\sigma\left[1-\frac{x}{(x^2+\rho_0^2)^{1/2}}\right]e^{-(t-x/V_s)/\tau_s}\,, \tag{19}$$

and the total energy becomes

$$E_t=\pi\rho_0^2\sigma\tau_s\,. \tag{20}$$

To prepare for a comparison to the data we convert Eq. (19) to a velocity relation through the drift relation from Eq. (1), $v_d=F\tau/m$, and replace σ by $E_t/\pi\rho_0^2\tau_s$. We now have

$$v_d(x,t)=\frac{\partial x}{\partial t}=\frac{2E_t\Phi}{\rho_0^2\tau_s}\left[1-\frac{x}{(x^2+\rho_0^2)^{1/2}}\right]e^{-(t-x/V_s)/\tau_s}\,. \tag{21}$$

The force on an electron-hole droplet due to the phonon wind is proportional to the net flux of phonons in the droplet frame of reference. For a droplet in motion with velocity V_d the effective force is reduced by a factor of $1-V_d/V_s$. This gives an effective velocity V_d in terms of Eq. (21) as

$$V_d=v_d/(1+v_d/V_s)\,. \tag{22}$$

In the limit of $v_d \ll V_s$ we recover the expected result $V_d=v_d$. We can see that V_d is limited to less than V_s. This effect is apparently observed in Fig. 15(a). Note that this particular velocity limit does not apply for droplets that are pushed by strain gradients. Equations (21) and (22) are somewhat awkward to handle analytically. They can be integrated in finite elements by a simple computer program. The resulting curves of x as a function of t are then fit to the data using E_t and τ_s as parameters. The resulting fit to the data and the energy, $E_t=E_{\rm fit}$, is shown in Fig. 13. The quantity $E_{\rm fit}$ is somewhat larger than the measured value, but clearly scales with it. The power dependence of the fitted storage time is shown in Fig. 16(a). These calculated storage times are comparable to those observed in a bolometer experiment examining the same effects under similar conditions.[30]

In Fig. 16(b), the fitted incident energy, $E_{\rm fit}$, is seen to be always about 3 times larger than the actual measured pulse energy, $E_{\rm inc}$. This indicates that the phonon-wind force parameter, Φ, is actually larger under these pulsed conditions than that obtained from continuous low-power excitation ($P_{\rm abs}\approx 100$ mW). For pulsed excitation, the implicit assumption is made that the phonon spectrum at large distances from the excitation region ($x\geq 0.5$ mm) is the same for all excitation levels. In other words, the total phonon-energy flux is proportional to the rate at which energy leaves the excitation region, while the phonon-frequency distribution remains unaffected. This assumption was borne out by experiments measuring the steady-state EHD cloud size for a continuously excited unstrained sample. The cloud size varied as $P_{\rm inc}^{1/3}$ for powers up to 0.2 W, indicating that the wind force was strictly proportional to incident power. However, in the pulsed case, phonon energy amounting to 10 μJ or more is released in a time of order 1 μs. This is equivalent to 10 W or more of instantaneous laser power. It is not unreasonable that under these conditions a greater proportion of this energy is down-

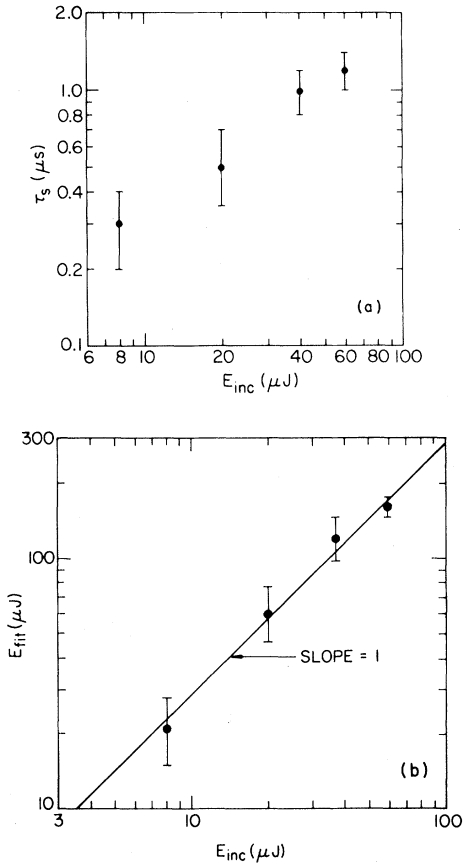

FIG. 16. (a) Dependence of the fitted storage time on pulse energy; (b) comparison of $E_{\rm fit}$ and $E_{\rm inc}$ from Fig. 12, illustrating the linear relation.

converted into the form of phonons that participate in drop transport, i.e., long-wavelength acoustic phonons. In light of the postulated storage effect, such an enhancement might be expected. If the heat storage effect was due to the reduction of the mean free path of high-frequency phonons, it would slowly convert the stored high-energy phonons, which cannot induce drop motion, into low-frequency phonons which can push drops. This phonon storage and down conversion should produce an enhancement of the phonon-wind force. Considering the 50-fold increase in instantaneous power, the low-power wind calibration is surprisingly accurate, within a factor of 3 in predicting cloud volume or a factor of $3^{1/3}=1.4$ in predicting cloud radius. The discrepancy suggests interesting physical differences in the phonon distributions produced by continuous and intense pulsed excitation.

VII. SUMMARY

In this work the transport of EHD has been examined over an extremely wide range of excitation intensities. At a low level of excitation the motion of EHD in a strain gradient was found to be entirely consistent with a linear drift relation, $\tau=mV_d/F$. We measured the temperature dependence of the damping time, $\tau=(1.06\ \text{ns K})/T$, which is in fairly close agreement with the phonon-scattering models of EHD momentum damping.

Near the excitation region, the drift velocity was found to be enhanced by a force due to the flux phonons produced by carrier thermalization. The strength of this phonon-wind force was directly measured by comparison to the strain-gradient force. The measured wind force for a given excitation power and the measured damping time were used to "predict" steady-state EHD cloud sizes, which were consistent with the observed cloud sizes in unstrained Ge.

Under intense pulsed (100 ns) excitation the EHD cloud was observed to grow in three stages. Apparently, a layer of electron-hole liquid was formed near the sample surface. Because the EHL is of constant density, the thickness of this layer was proportional to the pulse energy. This "jump-out" effect may explain the difficulty in measuring the initial drop size by light scattering, as encountered in Ref. 3. Our results indicate that the EHL is probably not in the form of small droplets at very early times. After this initial stage, the EHL then breaks away from the surface, driven by a force that decays with $\tau_s \approx 1\ \mu$s. This force is attributed to a flux of phonons emitted by a heated region near the sample surface. The observed storage time is consistent with times observed in recent bolometer experiments that detect the ballistic phonon flux directly.[30] The EHD motion in this persistent phonon wind is used to reconstruct the energy of the laser pulse using the cw phonon-wind parameter. The fitted pulse energies are about a factor of 3 larger than the measured pulse energies, and are found to be linear with them. The difference in efficiency for phonon-wind production in cw and pulsed cases is attributed to nonlinear phonon down conversion at higher instantaneous temperatures. The third gentle-growth stage observed in the cloud expansion is attributed to the flux of recombination phonons from the drops themselves.

Time-resolved images of the pulse-excited EHD cloud also showed the three expansion regimes. In addition, they displayed an anisotropy in the phonon-wind force due to phonon focusing. It was the persistence of these features that motivated the study of the local heat storage effects. An upper limit of $\lesssim 300\ \mu$m on the diameter of the region which the heat storage takes place is found from these time-resolved images. Unlike the steady-state cloud, directions of enhanced phonon flux appear in the pulse-excited cloud as regions of low droplet density. This is consistent with the "fill-in" effect, which was previously postulated to explain the large droplet concentrations in the high-phonon flux directions of the steady-state cloud.

In conclusion, the transport of EHD in Ge has been placed on a more quantitative basis for both strain-gradient and phonon-wind induced motions. These experiments complement a wide range of earlier results, and resolve several contradictions and discrepancies. With this understanding of the dynamics of EHD motion in a wide range of circumstances, the use of EHD as a reliable probe of nonequilibrium phonon fluxes is made possible.

ACKNOWLEDGMENTS

We wish to thank E. E. Haller for supplying the Ge samples. This project was supported in part by the National Science Foundation under Materials Research Laboratory Grant No. DMR-80-20250 and under Grant No. DMR-80-24000.

[1]For a general review of the properties of EHL, see J. C. Hensel, G. A. Thomas, T. G. Phillips, and T. M. Rice *Solid State Physics,* edited by H. Ehrenreich, F. Seitz, and D. Turnbull (Academic, New York), Vol. 32.

[2]M. Combescot, Phys. Rev. B 12, 1591 (1975).

[3]T. C. Damen and J. M. Worlock, in *Proceedings of the Third International Conference on Light Scattering in Solids, Campinas, 1975* (Flammarion, Paris, 1976), p. 183.

[4]V. S. Bagaev, L. V. Keldysh, N. N. Sibel'din, and V. A. Tsvetkov, Zh. Eksp. Teor. Fiz. 70, 702 (1976) [Sov. Phys.—JETP 43, 362 (1976)].

[5]L. V. Keldysh, Pis'ma Zh. Eksp. Teor. Fiz. 23, 100 (1976) [JETP Lett. 23, 87 (1976)].

[6]R. S. Markiewicz, Phys. Rev. B 21, 4674 (1978).

[7]R. C. Dynes and J. C. Hensel, Phys. Rev. Lett. 39, 969 (1977).

[8]M. Greenstein and J. P. Wolfe, Solid State Commun. 33, 309 (1980); Phys. Rev. Lett. 41, 715 (1978).

[9]M. Greenstein and J. P. Wolfe, Phys. Rev. B 24, 3318 (1981).

[10]M. A. Tamor and J. P. Wolfe, Phys. Rev. B 24, 3596 (1981).

[11]A. S. Alekseev, T. I. Galkina, V. M. Maslennikov, R. G. Khakamov, and E. E. Shchebnev, Pis'ma Zh. Eksp. Teor. Fiz. 21, 578 (1975) [JETP Lett. 21, 271 (1975)].

[12]A. D. A. Hansen, Ph.D. Thesis, University of California, Berkeley, 1977 (unpublished).

[13]A. S. Alekseev, T. A. Astimirov, V. S. Bagaev, T. I. Galkina, N. A. Penin, N. N. Sibel'din and V. A. Tsvetkov, in *Proceedings of the Twelth International Conference on Physics of Semiconductors, Stuttgart, 1974,* edited by M. H. Pilkuhn (Teubner, Stuttgart, 1974), p. 91.

[14]C. Herring and E. Vogt, Phys. Rev. 101, 944 (1956).

[15]L. V. Keldysh and S. G. Tikhoodeev, Pis'ma Zh. Eksp. Teor. Fiz. 21, 582 (1975) [JETP Lett. 21, 273 (1975)].

[16]M. A. Tamor and J. P. Wolfe, Phys. Rev. B 26, (1982).

[17]I. Balslev, Phys. Rev. 143, 636 (1966).

[18]K. Murase, E. Enjouji, and E. Otsuka, J. Phys. Soc. Jpn. 29, 1248 (1970).

[19]D. S. Pan, D. L. Smith, and T. C. McGill, Phys. Rev. B 17, 3284 (1978).

[20]R. S. Markiewicz, Phys. Status Solidi B 90, 585 (1978).

[21]M. I. D'yakonov and A. V. Subashiev, Zh. Eksp. Teor. Fiz. 75, 1943 (1978) [Sov. Phys.—JETP 45,(5), 980 (1978)].

[22]R. S. Markiewicz, J. P. Wolfe, and C. D. Jeffries, Phys. Rev. B 15, 1978 (1977).

[23]S. M. Kelso, Phys. Rev. B 25, 1116 (1982).

[24]M. Greenstein and J. P. Wolfe, Phys. Rev. Lett. 41, 715 (1978).

[25]G. A. Northrop and J. P. Wolfe, Phys. Rev. B 22, 6196 (1980).

[26]J. P. Wolfe, M. Greenstein, and G. A. Northrop, in Proceedings of the 15th International Conference on Physics of Semiconductors, Kyoto, 1980 [J. Phys. Soc. Jpn. (Suppl. A) 49, 491 (1980)].

[27]N. V. Zamkovets, N. N. Sibel'din, V. B. Stopachinskii, and V. A. Tsvetkov, Zh. Eksp. Teor. Fiz. 74, 1147 (1978) [Sov. Phys.—JETP 4, 603 (1978)].

[28]M. Combescot, Phys. Rev. B 12, 1591 (1975).

[29]G. Mahler, G. Maier, A. Forchel, B. Laurich, H. Sanwald, and W. Schmid Phys. Rev. Lett. 47, 1855 (1981). Also, A. Forchel *et al.* (unpublished).

[30]M. Greenstein, M. A. Tamor, and J. P. Wolfe, Phys. Rev. B 26, 5604 (1982).

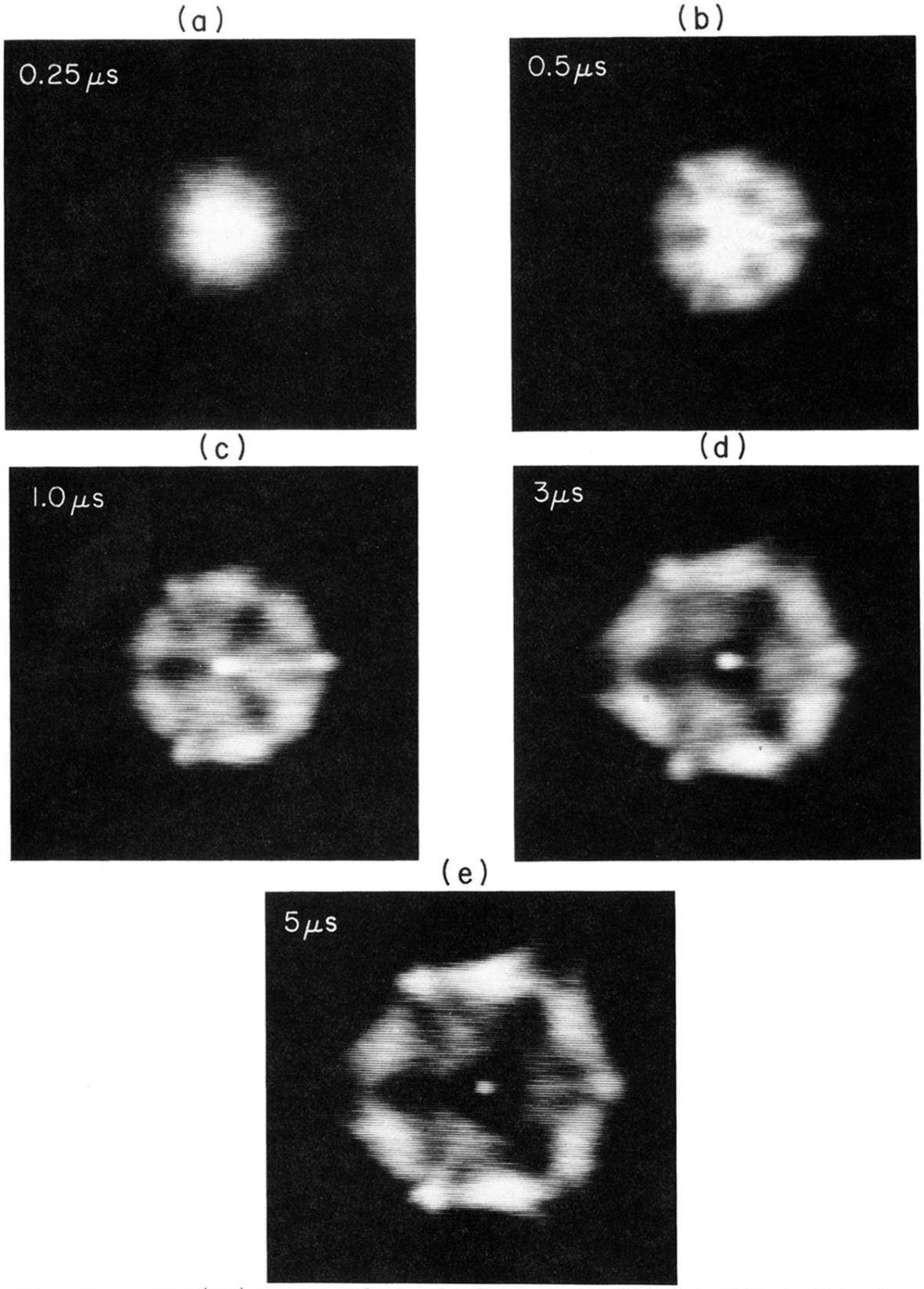

FIG. 11. Time-resolved ⟨100⟩ cloud images for $E_{inc}=20\ \mu J$. (a) $t=0.25\ \mu s$; (b) $t=0.5\ \mu s$; (c) $t=1\ \mu s$; (d) $t=3\ \mu s$; (e) $t=5\ \mu s$.

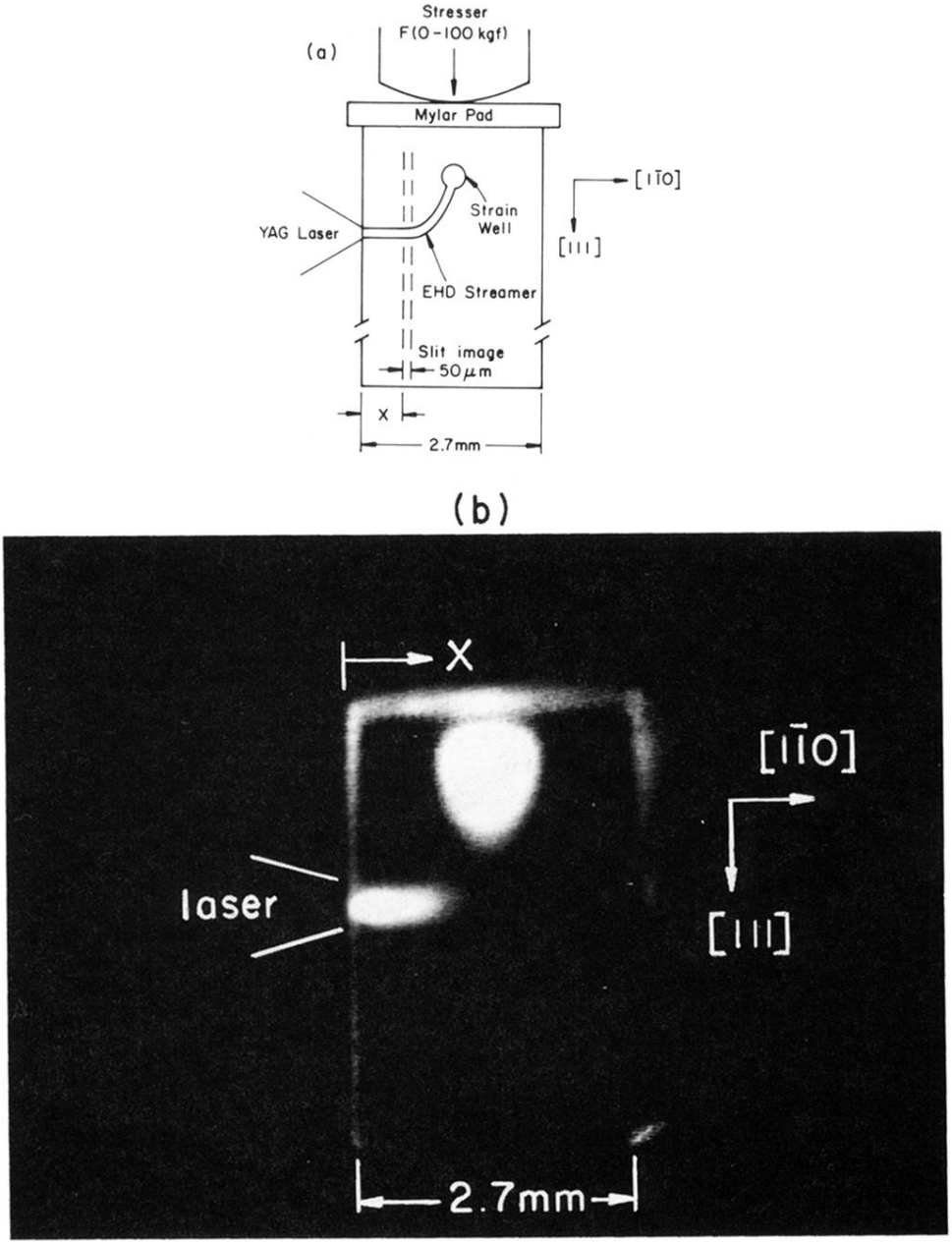

FIG. 3. (a) Schematic of the stress geometry and crystal orientation. (b) Luminescence image of the EHD streamer with low spectral resolution and continuous laser excitation.

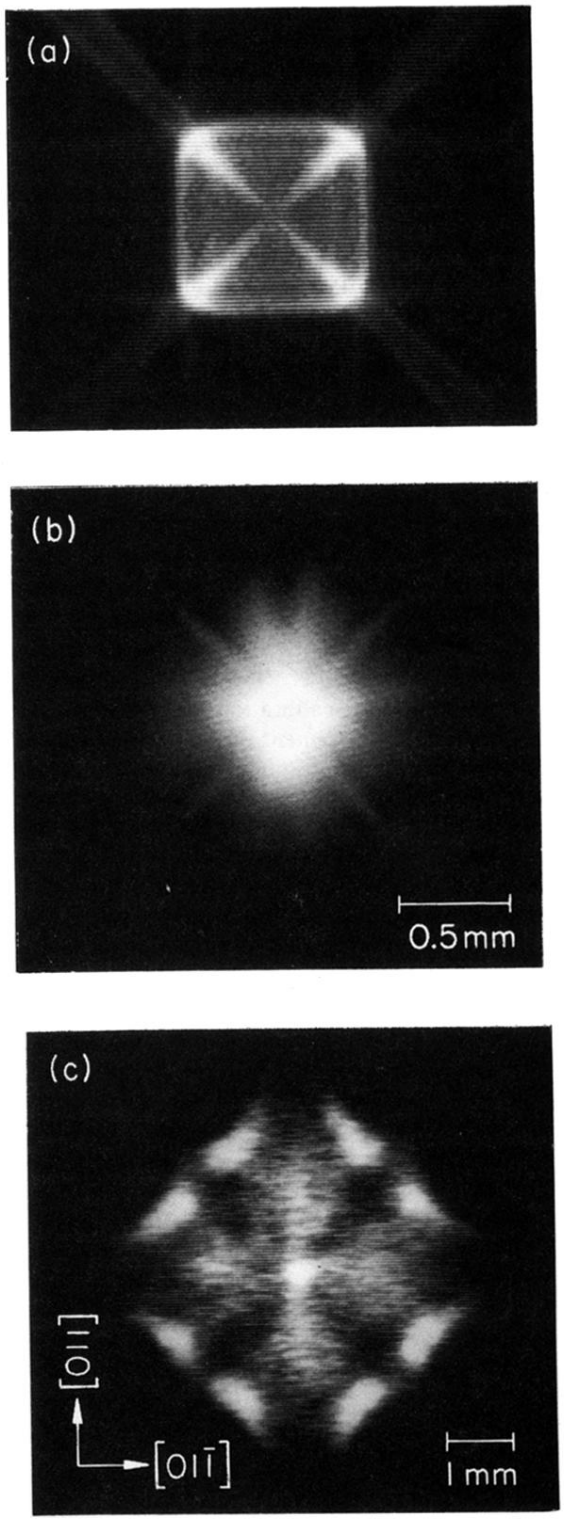

FIG. 8. (a) Ballistic phonon image in the ⟨100⟩ direction from Ref. 25; (b) steady-state ⟨100⟩ cloud image, $P_{\text{inc}}=76$ mW; (c) pulsed cloud (300-ns pulse width) taken at 5 μs after the excitation pulse with $E_{\text{inc}}=20\,\mu$J.

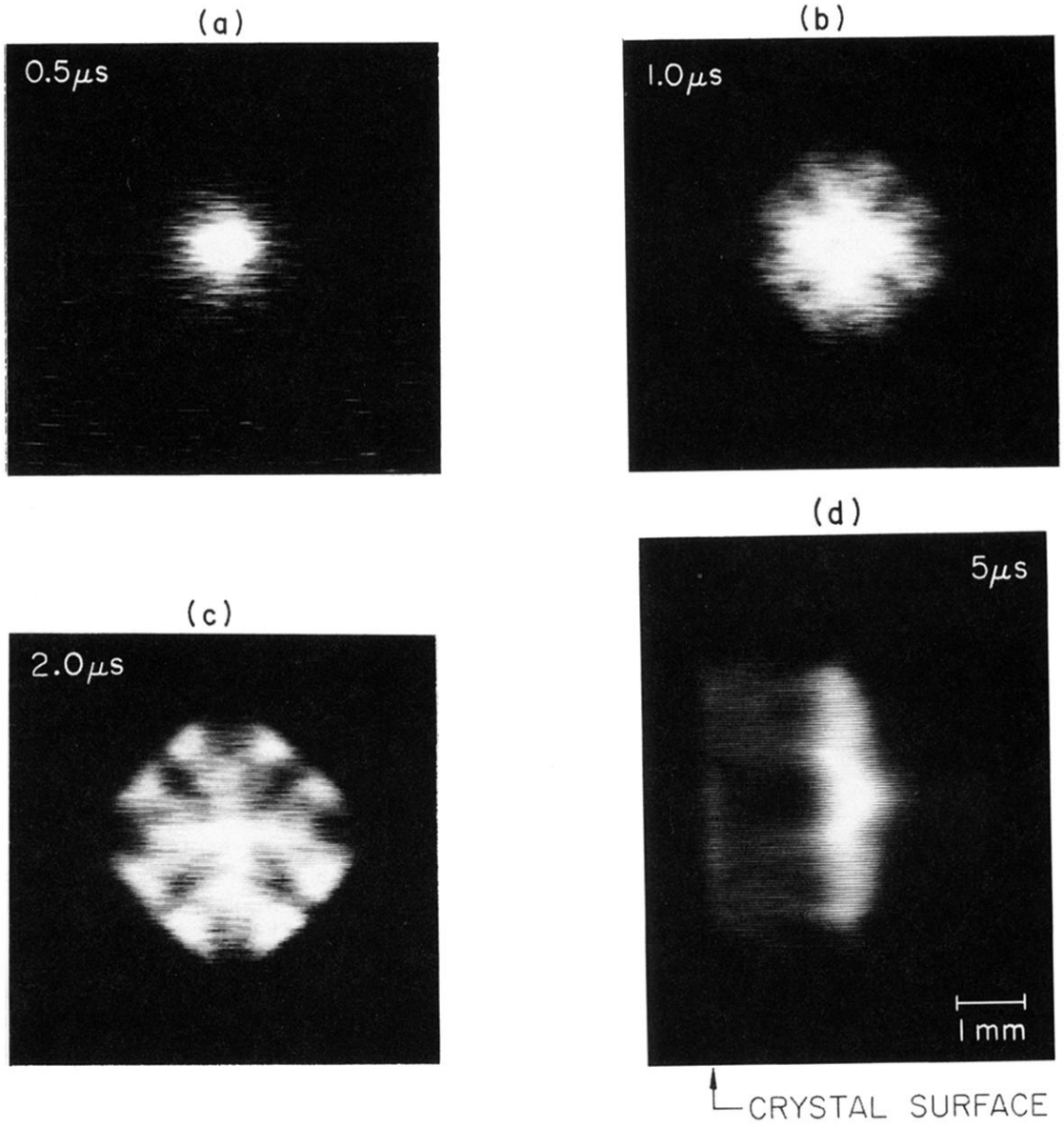

FIG. 9. Time-resolved ⟨100⟩ cloud image for 300-ns excitation. $E_{inc}=20\ \mu J$. (a) $t=0.5\ \mu s$; (b) $t=1\ \mu s$; (c) $t=2\ \mu s$; (d) side view of a time-resolved ⟨100⟩ cloud at $t=5\ \mu s$, $E_{inc}=20\ \mu J$.